Journal of
Materials Chemistry B

ROYAL SOCIETY
OF CHEMISTRY

PAPER

View Article Online
View Journal | View Issue

Cite this: *J. Mater. Chem. B*, 2024, **12**, 6605

# Tough and elastic hydrogels based on robust hydrophobicity-assisted metal ion coordination for flexible wearable devices†

Zheng Liu,‡[a] Kaixiang Shen,‡[a] Mengyuan Zhang,[a] Yuchen Zhang,[b] Zhuting Lv,[a] Qinghua Shang,[a] Renjie Li,[a] Can Zhou*[c] and Yilong Cheng *[ad]

Received 30th April 2024,
Accepted 5th June 2024

DOI: 10.1039/d4tb00933a

rsc.li/materials-b

Flexible wearable sensors that combine excellent flexibility, high elasticity, sensing capabilities, and outstanding biocompatibility are gaining increasing attention. In this study, we successfully develop a robust and elastic hydrogel-based flexible wearable sensor by modulating molecular structures combined with metal ion coordination. We leverage three *N*-acryloyl amino acid monomers, including *N*-acryloyl glycine (AG), *N*-acryloyl alanine (AA), and *N*-acryloyl valine (AV) with different hydrophobic groups adjacent to the carboxyl group, to copolymerize with acrylamide (AM) in the presence of $Zr^{4+}$ for hydrogel preparation in one step ($P(AM_3–AG/AA/AV_{0.06})–Zr_{0.03}{}^{4+}$ hydrogels). Our investigation reveals that the $P(AM_3–AV_{0.06})–Zr_{0.03}{}^{4+}$ hydrogel with the most hydrophobic side group demonstrates superior mechanical properties (1.1 MPa tensile stress, 3566 kJ $m^{-3}$ toughness and 1.3 kJ $m^{-2}$ fracture energy) and resilience to multiple tensile (30% strain, 500 cycles) and compression cycling (50% strain, 500 cycles). Moreover, the $P(AM_3–AV_{0.06})–Zr_{0.03}{}^{4+}$ hydrogel exhibits good biocompatibility and high conductivity (1.1 S $m^{-1}$) and responsivity (GF = 16.21), and is proved to be suitable as a flexible wearable sensor for comprehensive human activity monitoring.

## Introduction

Wearable sensors play a pivotal role in diverse domains such as human motion detection, physiological indicator monitoring,[1,2] clinical diagnosis,[3,4] and human–machine interaction.[5] The demand for wearability underscores the necessity for sensors capable of withstanding mechanical deformation, encompassing stretching, bending, folding, and twisting.[6] However, traditional sensors typically employ an elastic substrate filled with conductive materials, resulting in rigidity and limited mechanical deformability. This leads to reduced sensitivity, stability of signal transmission, and overall comfort in wearability.[7] Hydrogels, characterized as hydrophilic polymer networks with three-dimensional cross-linking structures using water as the dispersion medium, present a promising solution.[8,9] They are biocompatible and offer the ability to design and adjust mechanical properties, rendering them flexible and stretchable to mimic biological tissue mechanics.[10,11,12] However, due to the weak inter/intramolecular interactions, traditional hydrogels often lack the requisite strength and toughness for applications in wearable sensors, which usually

**Yilong Cheng**

*Dr Yilong Cheng is a professor in the School of Chemistry at Xi'an Jiaotong University. He obtained his B.S. degree in polymer chemistry from the University of Science and Technology of China in 2008 and completed his PhD study under the supervision of Prof. Xuesi Chen in Changchun Institute of Applied Chemistry in 2014. Then he joined Prof. Suzie Pun's group as a Postdoctoral Fellow at the University of Washington for polymeric gene vector design. His current research interest is the development of functional polymeric hydrogels for various biomedical applications.*

---

[a] *Engineering Research Center of Energy Storage Materials and Devices, Ministry of Education, School of Chemistry, Xi'an Jiaotong University, Xi'an 710049, China. E-mail: yilongcheng@mail.xjtu.edu.cn*

[b] *Key Laboratory of Shaanxi Province for Craniofacial Precision Medicine Research, College of Stomatology, Xi'an Jiaotong University, Xi'an 710049, China*

[c] *Breast Surgery Department, First Affiliated Hospital, Xi'an Jiaotong University, Xi'an 710049, China. E-mail: zhoucanz2005@126.com*

[d] *Department of Nuclear Medicine, the First Affiliated Hospital of China, Xi'an Jiaotong University, Xi'an 710049, China*

† Electronic supplementary information (ESI) available. See DOI: **https://doi.org/10.1039/d4tb00933a**

‡ These authors contributed equally to this work.

exhibit typical values of tensile stress around 10 kPa and fracture energy below 10 J $m^{-2}$.[13] Until now, various methods have been explored to enhance their mechanical properties, including the introduction of sacrificial bonds,[14,15] nanoparticles[16] and crystal structures.[17,18] Among them, the introduction of metal ion coordination interaction into the hydrogel network is one of the promising solutions because it can not only elevate the mechanical properties through the increased crosslinking density but also endow the hydrogels with desired conductivity.[19–22]

Lately, there has been rising interest in enhancing hydrogels' mechanical properties by introducing various metal ions into polymer networks, showcasing significant potential for applications in wearable flexible sensors.[23,24] $Fe^{3+}$ can coordinate with three $COO^-$ groups in the polymer network, which could serve as a potent cross-linking point to improve mechanical performances of hydrogels. Hu *et al.* immersed a hydrogel comprising poly(acrylamide-*co*-acrylic acid) mixed with clay nanosheets into a $Fe^{3+}$ solution to establish coordination cross-linking points between $Fe^{3+}$ and carboxyl groups. This approach resulted in the hydrogel exhibiting substantial tensile strain (2100%), excellent tensile stress (3.5 MPa), and commendable toughness (49 MJ $m^{-3}$).[25] Wang *et al.* introduced $Fe^{3+}$ into a copolymer network consisting of acrylamide, acrylonitrile, and maleic acid through soaking. The resulting hydrogel system exhibited a range of properties akin to those observed in flexible tissues, including high water content (~84%), low modulus of elasticity (0.06 MPa), high strength (1.4 MPa), high toughness (5.1 MJ $m^{-3}$), excellent strain-hardening ability, and robust self-recovery and fatigue resistance.[26] However, the preparation of the above-mentioned hydrogels usually involved two steps including polymerization and soaking processes, and the fast chelation between carboxyl groups and $Fe^{3+}$ on the

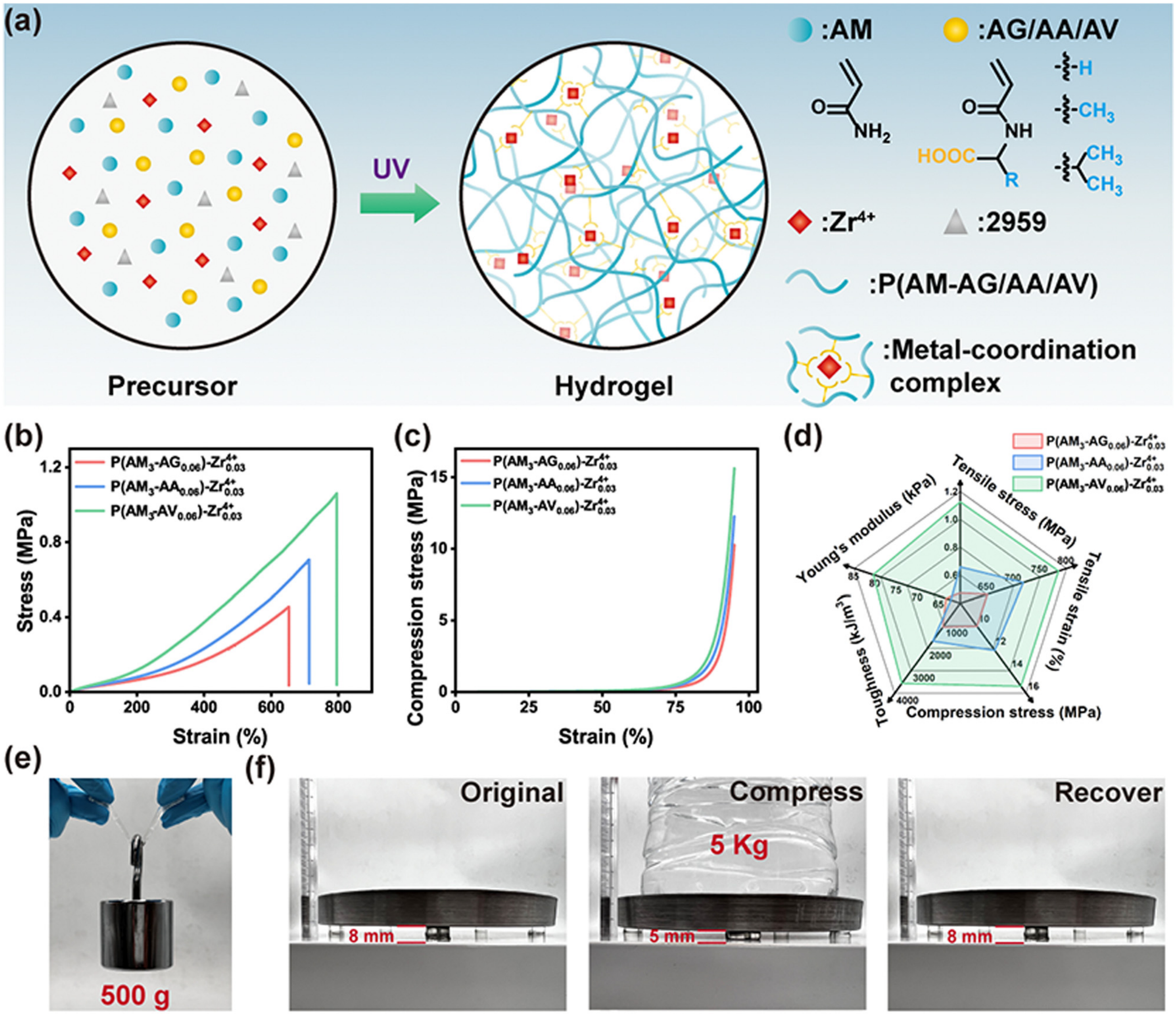

Fig. 1 (a) Schematic illustration of the preparation of $P(AM_3–AG/AA/AV_{0.06})–Zr_{0.03}{}^{4+}$ hydrogels. Tensile (b) and compression (c) stress–strain curves of $P(AM_3–AG/AA/AV_{0.06})–Zr_{0.03}{}^{4+}$ hydrogels. (d) Summaries of toughness, Young's modulus, tensile stress, tensile strain and compression stress of $P(AM_3–AG/AA/AV_{0.06})–Zr_{0.03}{}^{4+}$ hydrogels. Digital photographs of the $P(AM_3–AG/AA/AV_{0.06})–Zr_{0.03}{}^{4+}$ hydrogel weight bearing (e) and compression (f).

surfaces may lead to a nonuniform structure and poor mechanical performances due to the limited penetration of $Fe^{3+}$. Since $Fe^{3+}$ can potentially quench the free radicals during the gelation process, the addition of $Fe^{3+}$ into the initial solution is unfavourable for hydrogel fabrication by one-step polymerization.[27,28] Recently, Wu *et al.* developed a straightforward method to prepare tough hydrogels utilising $Zr^{4+}$ as the metal ion to chelate with $COO^-$ groups, and the resulting hydrogels exhibited tensile stress and Young's modulus in the ranges of 0.4–11.9 MPa and 0.07–186 MPa, respectively, which also showed vast potential in the applications of flexible wearable sensors and digital light processing 3D printing.[29] Moreover, the universality of $Zr^{4+}$–$COO^-$ coordination complexes to strengthen the mechanical performances of hydrogels has been verified in other polymerization systems using methacrylic acid, itaconic acid, aconitic acid, and maleic anhydride containing carboxyl groups.[29] However, the effect of the local chemical environment of the carboxyl group on the stability of the coordination complexes and further mechanical properties of the resulting hydrogel has not been studied.

In this study, we employed three *N*-acryloyl amino acid monomers, including *N*-acryloyl glycine (AG), *N*-acryloyl alanine (AA), and *N*-acryloyl valine (AV) with different hydrophobic groups adjacent to the carboxyl group, to copolymerize with acrylamide (AM) in the presence of $Zr^{4+}$ for hydrogel preparation in one step ($P(AM_3–AG/AA/AV_{0.06})–Zr_{0.03}{}^{4+}$ hydrogels, Fig. 1a). Due to the difference in the chemical environment of the COOH group, the resulting hydrogels showed distinct mechanical properties (tensile stress, tensile strain, compression stress, Young's modulus and toughness, Fig. 1b–d). We systematically evaluated the influence of the monomers and $Zr^{4+}$ concentrations on the mechanical performances of the hydrogels, and also compared the stability of the three coordination complexes using computational simulation to highlight the advantage of the $P(AM_3–AV_{0.06})–Zr_{0.03}{}^{4+}$ hydrogel. Moreover, the introduction of $Zr^{4+}$ conferred excellent electrical conductivity and sensitivity to the hydrogel, making it suitable as a flexible wearable sensor for daily human movement and physiological signal detection.

## Results and discussion

### Synthesis and characterization of $P(AM_3–AG/AA/AV_{0.06})–Zr_{0.03}{}^{4+}$ hydrogels

The successful synthesis of AG, AA and AV was confirmed by $^1H$ NMR and $^{13}C$ NMR spectra as shown in Fig. S1–S3 (ESI†). As depicted in Fig. 1a, the hydrogels were synthesized in a single step through photoinitiated radical copolymerization of precursor solutions composed of AM, AG/AA/AV, and $Zr^{4+}$ at room temperature. The resulting poly(AM-AG/AA/AV) chains were extensively crosslinked due to the *in situ* formation of robust $COO^-$ and $Zr^{4+}$ coordination complexes. The prepared hydrogel was designated as $P(AM_x\text{-}AG/AA/AV_y)–Zr_z{}^{4+}$, where $x$, $y$, and $z$ represented the incorporation concentration of AM, AG/AA/AV, and $Zr^{4+}$, respectively. As illustrated in Fig. S4 (ESI†), the peak at 1593 $cm^{-1}$ corresponding to the double bond disappeared after gelation, implying the completion of polymerization. Fig. 1b and c compared the uniaxial tensile and compressive properties of hydrogels formed with different ligands. The results demonstrated that as the hydrophobicity of the side group in the ligand increased, the mechanical properties of the hydrogels became more robust. Notably, hydrogels formed with the most hydrophobic ligand, AV, exhibited the best mechanical properties, including tensile strain of 785%, and maximum tensile and compressive stresses of 1.1 and 15.4 MPa, respectively. We then summarized the mechanical properties of the three hydrogels in Fig. 1d, which suggested that the presence of a hydrophobic group adjacent to the COOH group could significantly enhance the stability of the coordination complex and construct potent crosslinking points in the hydrogel network. Moreover, as shown in Fig. 1e and f, $P(AM_3–AV_{0.06})–Zr_{0.03}{}^{4+}$ hydrogel ($50 \times 8 \times 4$ $mm^3$) can withstand 500 g weight without fracture, and the compression displacement was only 37.5% when subjected to 5 kg weight (hydrogel size, $d$ = 12 mm, $h$ = 8 mm), which could quickly return to its original height upon weight removal.

The outstanding mechanical properties of the hydrogels may be attributed to the formation of robust metal coordination complexes between the $COO^-$ on the polymer side chains and $Zr^{4+}$. At a macroscopic level, we found that the $P(AM_3–AG/AA/AV_{0.06})$ hydrogel displayed low storage moduli ($G'$) was too soft to maintain the integrity due to the weak inter/intramolecular interaction (Fig. 2a and Fig. S5, ESI†); comparatively, the incorporation of $Zr^{4+}$ into the polymer system obviously enhanced the stability of the noncovalent-mediated hydrogels, which could be easily removed from the moulds with initial shape. We then employed FTIR and Raman spectra to verify the formation of coordination complexes. It was found that, compared to $P(AM_3–AG/AA/AV_{0.06})$ hydrogels, the peaks attributed to the symmetric stretching vibration of the $COO^-$ group shifted to higher wavenumbers following the addition of $Zr^{4+}$ (Fig. 2b).[30] Moreover, Raman spectra analysis further confirms the formation of $COO^-$–$Zr^{4+}$ coordination complex species (Fig. 2c). The peak positions of the $COO^-$ groups in the Raman spectra of the hydrogels toughened with $Zr^{4+}$ shift from ∼1311 and ∼1596 to ∼1320 and ∼1600 $cm^{-1}$, respectively, in comparison to the $P(AM_3–AG/AA/AV_{0.06})$ hydrogels without $Zr^{4+}$.[31] These spectral shifts provide compelling evidence for the formation of $COO^-$–$Zr^{4+}$ coordination complexes, further elucidating the enhanced mechanical properties observed in the hydrogel system. The formation of carboxylate–$Zr^{4+}$ coordination bonds was also confirmed by the appearance of a peak at 531.2 eV in the split-peak fit of the O1s orbital (Fig. S6, ESI†). Additionally, the deconvoluted Zr3d spectra exhibited two binding energies at 182.7 eV and 185.1 eV corresponding to $Zr3d_{5/2}$ and $Zr3d_{3/2}$, respectively.[29] These results revealed that the $COO^-$ groups on the side chains of P(AM–AG/AA/AV) could form coordination complexes with $Zr^{4+}$, which served as potent crosslinking points in the network to endow the hydrogels with promising mechanical performances.

Owing to the different hydrophobicity of the side group, it is expected that the $P(AM_3–AG/AA/AV_{0.06})–Zr_{0.03}{}^{4+}$ hydrogels

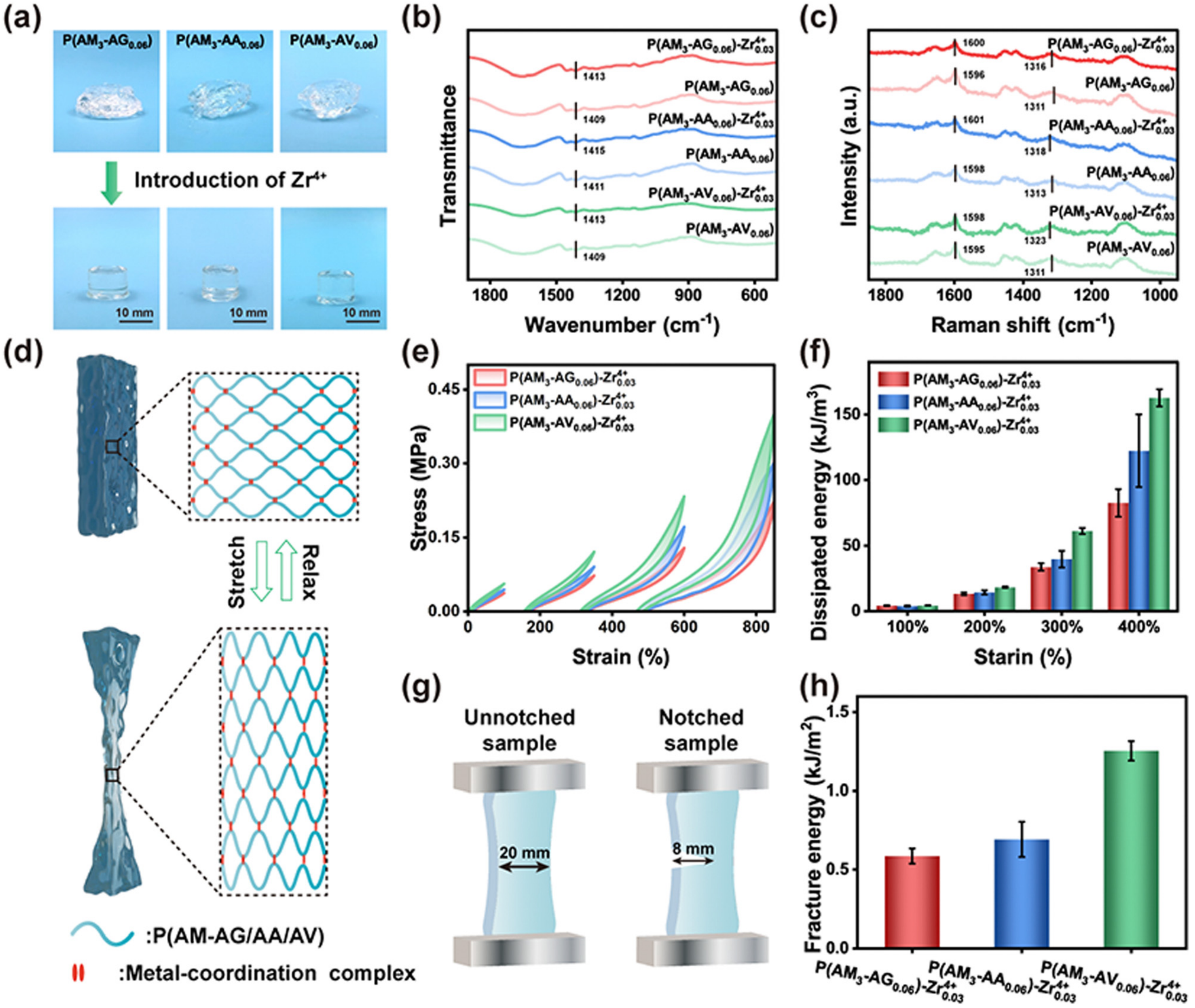

Fig. 2 (a) Digital photographs of changes in the hydrogel morphology before and after the introduction of $Zr^{4+}$. FTIR (b) and Raman (c) spectra of hydrogels before and after the introduction of $Zr^{4+}$. (d) Schematic representation of metal-coordination complexes in hydrogel stretching processes. Uniaxial stretching-relaxation cycle curves (e) and dissipated energy statistics (f). Notch sensitivity tests schematic (g) and fracture energy statistics (h).

should feature distinct mechanical properties. First, we studied the swelling ratios of the three hydrogels to indirectly reflect the crosslinking density. It was found in Fig. S7 (ESI†) that the swelling ratios were obviously different: the $P(AM_3–AV_{0.06})–Zr_{0.03}{}^{4+}$ hydrogel characterized by the most hydrophobic group on the ligand side chains exhibited the lowest swelling rate (134%); the swelling ratio for $P(AM_3–AG_{0.06})–Zr_{0.03}{}^{4+}$ and $P(AM_3–AA_{0.06})–Zr_{0.03}{}^{4+}$ hydrogels was 187% and 154%, respectively. The results underscored the regulatory role of ligand molecular structure in modulating the coordination strength of $COO^-$ with $Zr^{4+}$, thereby enhancing cross-linking density within the hydrogel network and resisting water molecule infiltration.[21] Further rheological testing was conducted to explore how the molecular structure of the monomers affected the mechanical properties of the hydrogel at room temperature (Fig. S5, ESI†). It was observed that the storage moduli ($G'$) of the hydrogels were all higher than the loss moduli, indicating the formation of a stable hydrogel network. Moreover, the $G'$ increased alongside the augmentation of hydrophobic groups on the side chains, in which $P(AM_3–AV_{0.06})–Zr_{0.03}{}^{4+}$ hydrogel demonstrated the highest modulus. These results were consistent with the tensile and compressive tests as previously mentioned in Fig. 1b and c, and indicated the positive correlation between the increase in hydrophobic functional groups and the enhancement of hydrogel mechanical properties.

The introduction of ligand cross-linking sites between $COO^-$ and $Zr^{4+}$ within the polymer network was performed *in situ*, aiming to improve the mechanical strength and toughness of the hydrogels, as illustrated in Fig. 2d. We then investigated the energy dissipation capability of the three hydrogels by analysing stress–strain curves during tensile-relaxation cycles. As illustrated in Fig. 2e, the area of the hysteresis loop expanded with increasing strain, which indicated that the hydrogels dissipated more energy due to the dissociation of hydrogen bonds and coordination complexes under larger strain during the deformation process. The magnitude of energy dissipation correlated with the binding strength and reattachment rate of the cross-linking sites.[32] The smaller hysteresis loops observed for $P(AM_3–AG/AA_{0.06})–Zr_{0.03}{}^{4+}$ hydrogels from 100% to 500% strain suggested the weaker binding strength of $AG–Zr^{4+}$ and $AA–Zr^{4+}$ ligand complexes. In contrast, owing to the high binding strength of $AV–Zr^{4+}$ coordination complexes, the $P(AM_3–AV_{0.06})–Zr_{0.03}{}^{4+}$ hydrogel exhibited more pronounced hysteresis phenomena and the largest dissipation energy in the stress–strain curves, as shown in Fig. 2f. The fracture toughness of $P(AM_3–AG/AA/AV_{0.06})–Zr_{0.03}{}^{4+}$ hydrogels was further evaluated through notch sensitivity test to highlight the advantage of $AV–Zr^{4+}$ coordination complexes (Fig. 2g). Notably, the $P(AM_3–AV_{0.06})–Zr_{0.03}{}^{4+}$ hydrogel with fracture energy as high as 1.3 kJ $m^{-2}$, demonstrating superior notch insensitive behaviour compared to $P(AM_3–AG_{0.06})–Zr_{0.03}{}^{4+}$ (0.6 kJ $m^{-2}$) and $P(AM_3–AA_{0.06})–Zr_{0.03}{}^{4+}$ (0.7 kJ $m^{-2}$) hydrogels (Fig. 2h and Fig. S8, ESI†). This finding indicated that the $AV–Zr^{4+}$ coordination complexes in the hydrogel network could efficiently prevent crack growth and significantly enhance the toughness of the hydrogel.

## Characterization of $AG/AA/AV–Zr^{4+}$ coordination

To comprehend the influence of ligand molecular structure on the enhancement and toughening mechanism of the coordination complexes mediated hydrogels, we initially examined the microscopic morphology of $P(AM_3–AG/AA/AV_{0.06})–Zr_{0.03}{}^{4+}$ hydrogels. Our observations revealed that all three hydrogel types exhibited continuous porous microstructures, yet there was a notable discrepancy in the pore size of the gel networks (Fig. 3a). Specifically, the pore size of the hydrogels decreased as the hydrophobicity of the side group increased, in which the $P(AM_3–AV_{0.06})–Zr_{0.03}{}^{4+}$ hydrogel exhibited the pore size as small as 2 μm (Fig. 3b). This phenomenon was attributed to the fact that the coordination complex formed by AV and $Zr^{4+}$ could efficiently crosslink the polymer chains and densify the microstructure of hydrogels. Furthermore, we designed a series of complex systems with a molar ratio of 2 : 1 for AG/AA/AV and $Zr^{4+}$ to theoretically analyse the binding strength. We determined the lowest energy configurations through structural optimization and calculated the binding energies, as depicted in Fig. 3c. It was evident that all three ligands form a tetra-coordination bond with $Zr^{4+}$, and the $AV–Zr^{4+}$ composite system exhibited the highest binding energy of 354.74 kcal $mol^{-1}$, followed by $AA–Zr^{4+}$ of 350.66 kcal $mol^{-1}$

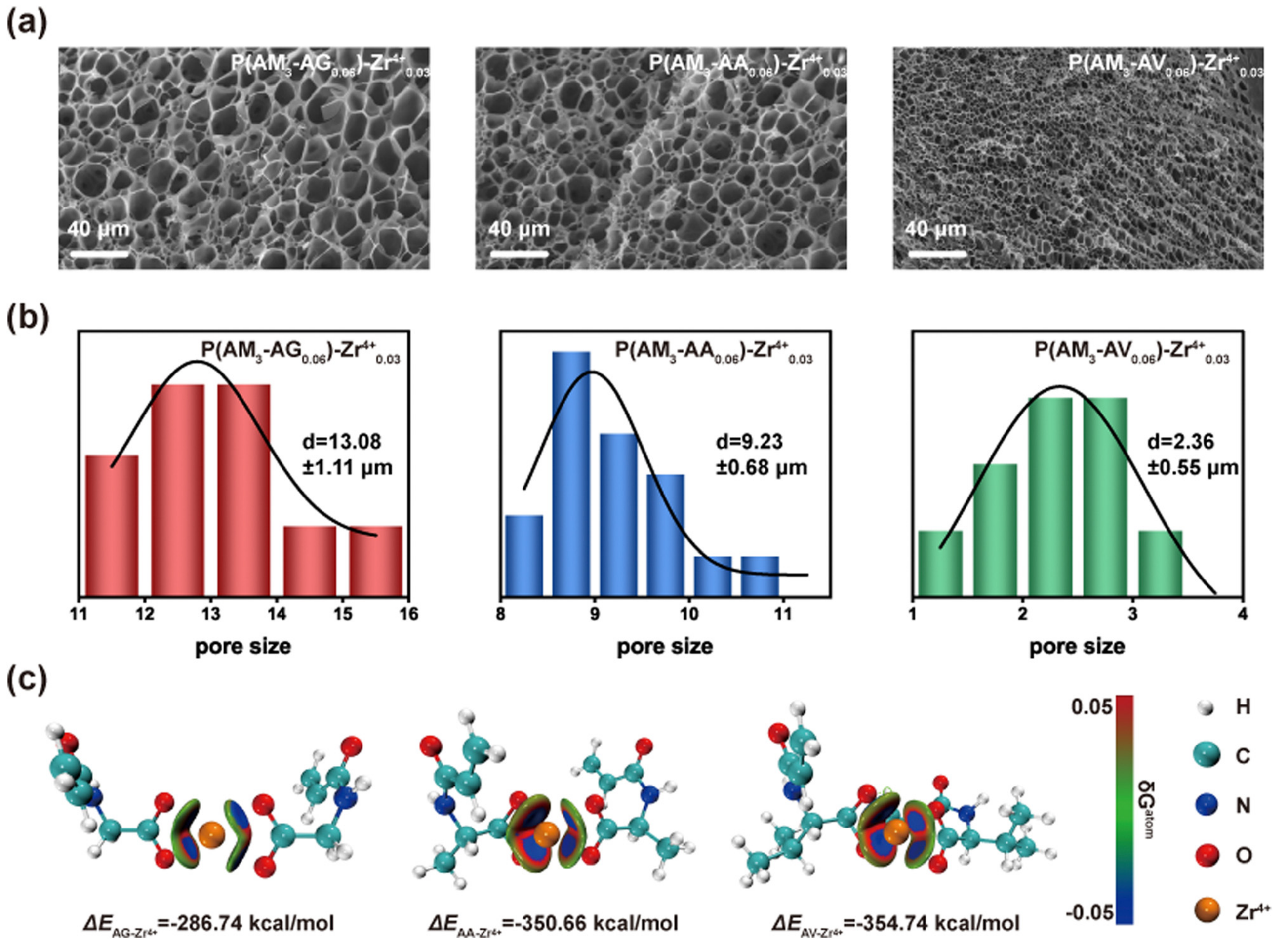

Fig. 3 SEM images (a) and pore size distribution statistics (b) of $P(AM_3–AG/AA/AV_{0.06})–Zr_{0.03}{}^{4+}$ hydrogels. (c) Computer optimized structures and binding energy of $AG/AA/AV–Zr^{4+}$ coordination complexes.

and AG–$Zr^{4+}$ of 286.74 kcal $mol^{-1}$. Therefore, we can conclude that the hydrophobic group adjacent to the $COO^-$ group could stabilize the coordination complexes formation, and the higher hydrophobicity of the side group could lead to the stronger binding strength between $COO^-$ and $Zr^{4+}$, by which the mechanical properties of the hydrogels can be facilely manipulated through the modulation of the chemical structure of ligand molecules. Based on the advantage in mechanical performances by $P(AM_3–AV_{0.06})–Zr_{0.03}{}^{4+}$ hydrogel, it is selected for further evaluation.

### Mechanical properties of $P(AM_3–AV_{0.06})–Zr_{0.03}{}^{4+}$ hydrogels

In the subsequent study, we evaluated the influence of AV and $Zr^{4+}$ concentrations on the mechanical properties of $P(AM_3–AV_y)–Zr_z{}^{4+}$ hydrogels. As illustrated in Fig. 4a, the tensile strength and strain of the hydrogels exhibited an initial increase followed by a decrease with escalating AV concentration from 0.02 M to 0.08 M. The peak values were attained at an AV concentration of 0.06 M, registering at 1.1 MPa for tensile strength and 785% strain, respectively. On the other hand, as the $Zr^{4+}$ concentration increased from 0.02 M to 0.05 M (the concentration of AV was set as 0.06 M), the hydrogel modulus gradually increased due to heightened metal–ligand bond density, and the stress *versus* strain graph displayed an initial rise and subsequent decline, reaching the pinnacle at a $Zr^{4+}$ concentration of 0.03 M (Fig. 4c). The augmentation in hydrogel mechanical properties associated with elevated AV and $Zr^{4+}$ content can be attributed to increased physical crosslink density. However, when the concentration of AV and $Zr^{4+}$ surpassed 0.06 M and 0.03 M, respectively, there was a reduction in the hydrogels' fracture stress and strain, which was likely due to the enhanced rigidity of the network to diminish hydrogel flexibility.[18] Regarding compressive properties, the compressive strength at a strain of 95% progressively rose with increasing AV and $Zr^{4+}$ concentrations, which was as high as 23 MPa when the concentration of AV and $Zr^{4+}$ was 0.06 and 0.05 M, respectively (Fig. 4b and d). Notably, the $P(AM_3–AV_{0.02})–Zr_{0.03}{}^{4+}$ hydrogel fractured before reaching 95% strain due to its lower density of physical cross-linking.

The recovery properties of $P(AM_3–AV_{0.06})–Zr_{0.03}{}^{4+}$ hydrogels were then investigated by subjecting them to tensile loading–unloading cycles with varied waiting times (Fig. 4e). It was found that the hydrogel achieved maximum stress of 100 kPa at the first tensile cycle (200% of strain) with relatively large hysteresis, indicating effective energy dissipation during the loading–unloading cycle.[33] The recoveries of maximum stress and dissipated energy for each cycle are depicted in Fig. 4f.

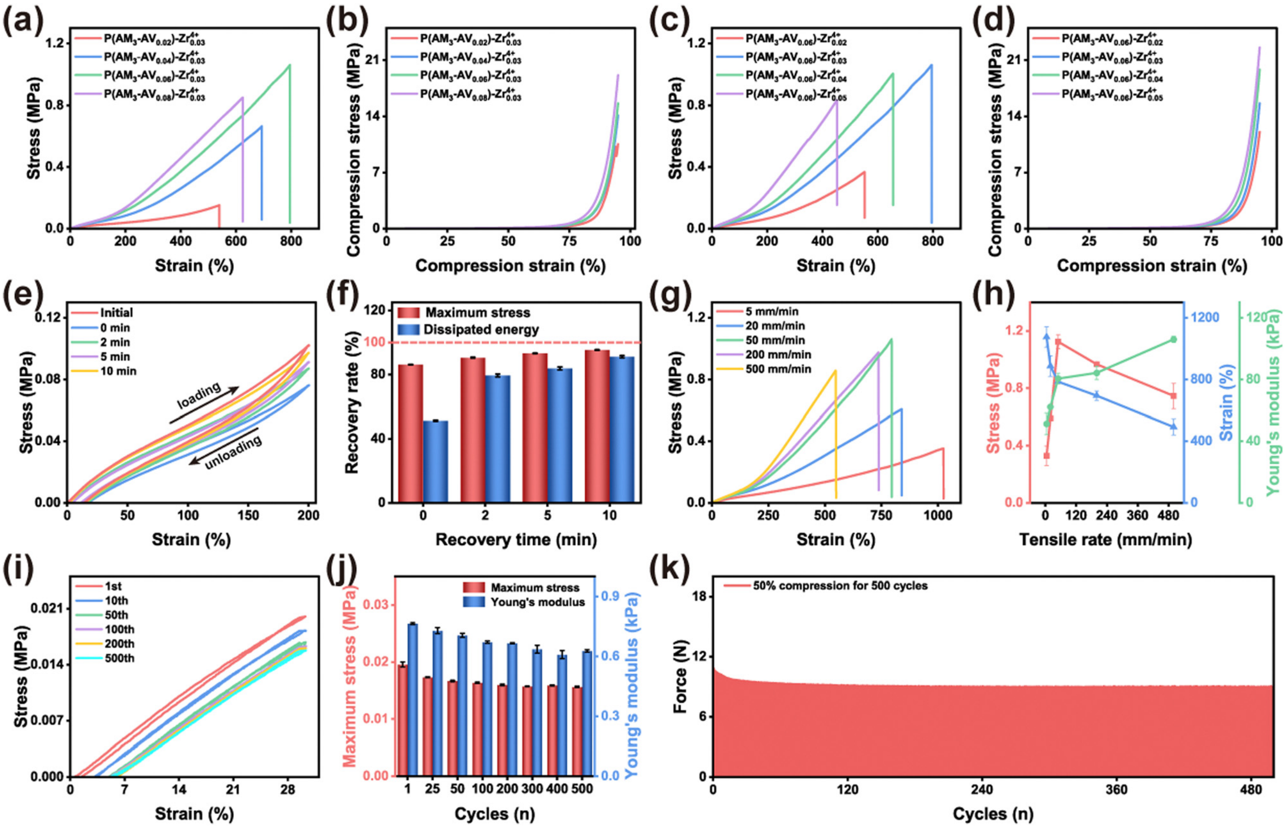

Fig. 4 Tensile (a) and compression (b) stress–strain curves of the $P(AM_3–AV_{0.06})–Zr_{0.03}{}^{4+}$ hydrogel with different AV concentrations. Tensile (c) and compression (d) stress–strain curves of the $P(AM_3–AV_{0.06})–Zr_{0.03}{}^{4+}$ hydrogel with different $Zr^{4+}$ concentrations. The loading–unloading curves at the strain of 200% (e) and the recovery ratio (f) of the $P(AM_3–AV_{0.06})–Zr_{0.03}{}^{4+}$ hydrogel after different resting times. Tensile stress–strain curves (g) and corresponding mechanical properties (h) of the $P(AM_3–AV_{0.06})–Zr_{0.03}{}^{4+}$ hydrogel at different tensile rates. Cyclic tensile stress–strain curves (i) and corresponding mechanical properties (j) of the $P(AM_3–AV_{0.06})–Zr_{0.03}{}^{4+}$ hydrogel. (k) Cyclic compression mechanical properties of the $P(AM_3–AV_{0.06})–Zr_{0.03}{}^{4+}$ hydrogel.

Notably, after a 10-minute waiting period, the recovery of dissipated energy and maximum stress reached 95% and 91%, respectively. This rapid recovery of mechanical properties is likely attributed to the swift reformation of metal–ligand cross-linking sites.[32]

The mechanical properties of the reinforced hydrogels were influenced by the tensile rate due to the dynamic behaviour of the metal–ligand complexes.[34] Upon increasing the tensile rate from 5 to 500 mm $\text{min}^{-1}$, Young's modulus of the hydrogel at room temperature rose from 51.2 to 106 kPa. Meanwhile, the tensile strain decreased from 1075% to 492%, and the tensile strength initially increased and then decreased, peaking at a tensile rate of 50 mm $\text{min}^{-1}$ (Fig. 4g and h). The observed effect of tensile rate on the hydrogels' mechanical properties primarily stems from the heightened binding strength of the ligands with increasing tensile rate.[35] At higher stretching rates, there is a delay in the dissociative rearrangement of the ligand bonds compared to the macroscopic deformation. During this time, physical cross-linking sites supply the energy needed to resist deformation, resulting in an increase in modulus and a decrease in tensile strain.

The fatigue resistance of the $\text{P(AM}_3\text{–AV}_{0.06}\text{)–Zr}_{0.03}{}^{4+}$ hydrogel was assessed through the application of 500 consecutive tensile-relaxation cycles and compression–relaxation cycles. The outcomes presented in Fig. 4i revealed that the maximum stress during the first 50 cycles slightly decreased, attributed to the partial dissociation of metal–ligand bonds within the hydrogel network. Subsequently, the maximum force of the hydrogel was sustained at 83% of its initial value, while the residual strain remained nearly unchanged (Fig. 4i, j and Fig. S9, ESI†). Additionally, the stress and strain curves almost overlapped, indicating that the equilibrium between dissociation and reorganization of metal–ligand bonds within the gel was sufficient to uphold the stability of mechanical properties across multiple tensile-relaxation cycles.[32] Fig. 4k and Fig. S10a, b (ESI†) illustrated the compression–relaxation cycles of $\text{P(AM}_3\text{–AV}_{0.06}\text{)–Zr}_{0.03}{}^{4+}$ hydrogels at 50% compressive strain, and the results showed that the maximum force remained constant for 500 consecutive cycles. In summary, the $\text{P(AM}_3\text{–AV}_{0.06}\text{)–Zr}_{0.03}{}^{4+}$ hydrogel exhibited exceptional elasticity, stability, and durability throughout both tensile and compression cycles, highlighting its potential for applications requiring long-term mechanical performance.

### Conductivity and sensing properties of $\text{P(AM}_3\text{–AV}_{0.06}\text{)–Zr}_{0.03}{}^{4+}$ hydrogels

In addition to enhancing the toughness of the hydrogel, the incorporation of $\text{Zr}^{4+}$ can induce the generation of electric current within the hydrogel, which imparts excellent electrical conductivity to the hydrogel (1.1 S $\text{m}^{-1}$, Fig. S11, ESI†).[36] The sensitivity of the hydrogel as a flexible wearable sensor can be evaluated using the gauge factor (GF), as illustrated in Fig. 5a. The $\text{P(AM}_3\text{–AV}_{0.06}\text{)–Zr}_{0.03}{}^{4+}$ hydrogel demonstrated remarkable sensitivity and a broad sensing range during stretching. Additionally, the relative resistance change exhibited varied response sensitivities across different strain ranges, with values reaching 4.12 (0–200%), 9.03 (200–600%), and 16.21 (600–800%) by fitting the GF curves through three linear regressions, respectively. It's noteworthy that the GF reached as high as 16.21 when the strain reached 800%, which surpassed most of the corresponding GFs in previously reported hydrogel-based flexible wearable sensors.[14,21,37] Furthermore, we investigated the electrical response of the hydrogel to cyclic stretching at different strains. As depicted in Fig. 5b, the hydrogel demonstrated precise and sensitive monitoring of the change in electrical resistance under small strains (1–5%) and large strains (50–300%). The output electrochemical signals remained stable and continuous during repetitive processes. Moreover, the $\text{P(AM}_3\text{–AV}_{0.06}\text{)–Zr}_{0.03}{}^{4+}$ hydrogel exhibited rapid electromechanical responsiveness, with response and recovery times of 35 and 21 ms, respectively (Fig. 5c). These response times were faster than human skin ($\sim$100 ms), enabling real-time monitoring of electrochemical signal changes by the hydrogel.[38] Importantly, the rate of change in electrical resistance of the $\text{P(AM}_3\text{–AV}_{0.06}\text{)–Zr}_{0.03}{}^{4+}$ hydrogel did not significantly decay during 500 cyclic sensing experiments with 100% tensile strain (Fig. 5d), indicating excellent stability and durability.

The $\text{P(AM}_3\text{–AV}_{0.06}\text{)–Zr}_{0.03}{}^{4+}$ hydrogel also exhibited multi-level response behaviour to changes in vertical pressure (Fig. 5e). The pressure sensitivity ($S$) was determined to be 0.0137, 0.0039, and 0.0023 $\text{kPa}^{-1}$ for the pressure ranges of 0–20, 20–50, and 50–100 kPa, respectively, which was promising for the monitoring of electrical signals under various stress conditions. Additionally, the hydrogel demonstrated a broad range of electrical signals in response to tiny (1 kPa) and large (80 kPa) stresses, and the output remained stable over multiple cycles, demonstrating sensitive, accurate and stable electrical signal responses (Fig. 5f). Moreover, we found that the successive application of compression stress (20 kPa) could output stable electrical signals correspondingly (Fig. 5g) indicating the real-time responsiveness of the hydrogel.[39] Furthermore, the durability of the $\text{P(AM}_3\text{–AV}_{0.06}\text{)–Zr}_{0.03}{}^{4+}$ hydrogel was assessed through 500 cycles of 20 kPa compression sensing experiments (Fig. 5h). The results revealed no significant shift or fluctuation in the relative resistance change during the cyclic test.

The remarkable sensitivity and long-term stability in strain and pressure sensing by $\text{P(AM}_3\text{–AV}_{0.06}\text{)–Zr}_{0.03}{}^{4+}$ hydrogel were owned to the good electrical conductivity of $\text{Zr}^{4+}$ combined with inherent excellent mechanical stability and anti-fatigue properties. Overall, these findings highlight the hydrogel's potential for applications in flexible wearable devices.

### Biocompatibility of $\text{P(AM}_3\text{–AV}_{0.06}\text{)–Zr}_{0.03}{}^{4+}$ hydrogels

Flexible wearable devices must prioritize excellent biosafety to be safely used for human activity monitoring. To assess the cytocompatibility of $\text{P(AM}_3\text{–AV}_{0.06}\text{)–Zr}_{0.03}{}^{4+}$ hydrogel, we initially conducted the 3-(4,5-dimethyl-2-thiazolyl)-2,5-diphenyl-2H-bromotetrazole (MTT) assay (Fig. 6a) using L929 cells incubated with the hydrogel leaching solution. The results showed that the cells proliferated well with the stimulation of $\text{P(AM}_3\text{–AV}_{0.06}\text{)–Zr}_{0.03}{}^{4+}$ hydrogel, and there was no significant difference found between the experimental and the control group. Moreover, we evaluated the cytotoxicity of the hydrogel using Live-Dead staining assay.

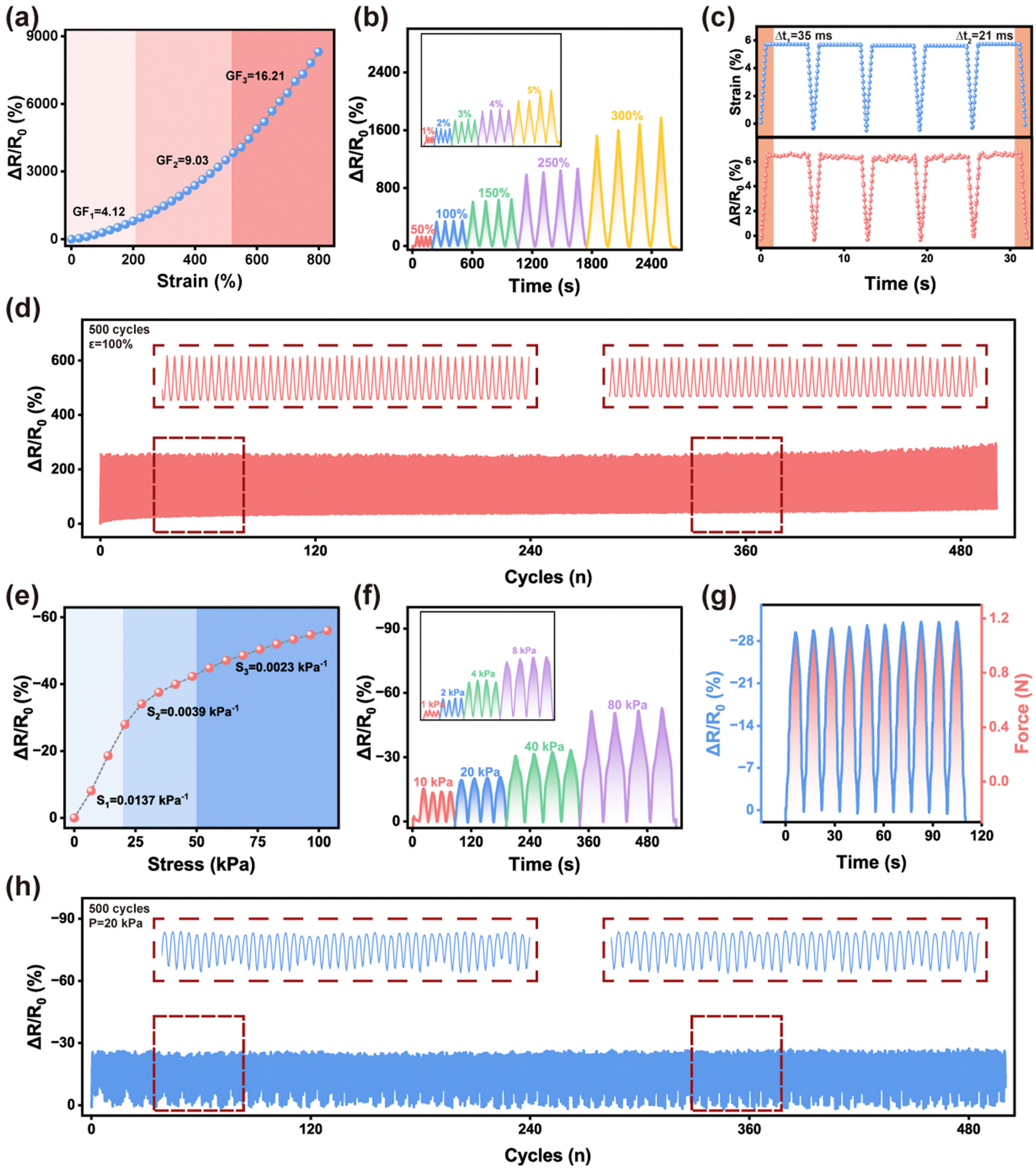

Fig. 5 (a) $\Delta R/R_0$ of the P(AM$_3$–AV$_{0.06}$)–Zr$_{0.03}$$^{4+}$ hydrogel in response to tensile strain. (b) $\Delta R/R_0$ of the P(AM$_3$–AV$_{0.06}$)–Zr$_{0.03}$$^{4+}$ hydrogel with different strains. (c) Tensile strain–time curve and the corresponding $\Delta R/R_0$–time curve of the P(AM$_3$–AV$_{0.06}$)–Zr$_{0.03}$$^{4+}$ hydrogel. (d) Cycling stability of the P(AM$_3$–AV$_{0.06}$)–Zr$_{0.03}$$^{4+}$ hydrogel under 100% tensile strain for 500 cycles. (e) $\Delta R/R_0$ of the P(AM$_3$–AV$_{0.06}$)–Zr$_{0.03}$$^{4+}$ hydrogel in response to pressure. (f) $\Delta R/R_0$ of the P(AM$_3$–AV$_{0.06}$)–Zr$_{0.03}$$^{4+}$ hydrogel under different pressures. (g) Compression stress–time curve and the corresponding $\Delta R/R_0$–time curve of the P(AM$_3$–AV$_{0.06}$)–Zr$_{0.03}$$^{4+}$ hydrogel. (h) Cycling stability of the P(AM$_3$–AV$_{0.06}$)–Zr$_{0.03}$$^{4+}$ hydrogel under 20 kPa pressure for 500 cycles.

Live cells were indicated by green fluorescence, while dead cells were represented by red fluorescence (Fig. 6b). The hydrogel extract-treated group showed minimal red fluorescence, and the cell proliferation trend and morphology were almost as same as the control group, which suggested the excellent cytocompatibility of the P(AM$_3$–AV$_{0.06}$)–Zr$_{0.03}$$^{4+}$ hydrogel.

Furthermore, we assessed the *in vivo* histocompatibility of the hydrogel through subcutaneous implantation on mice, and

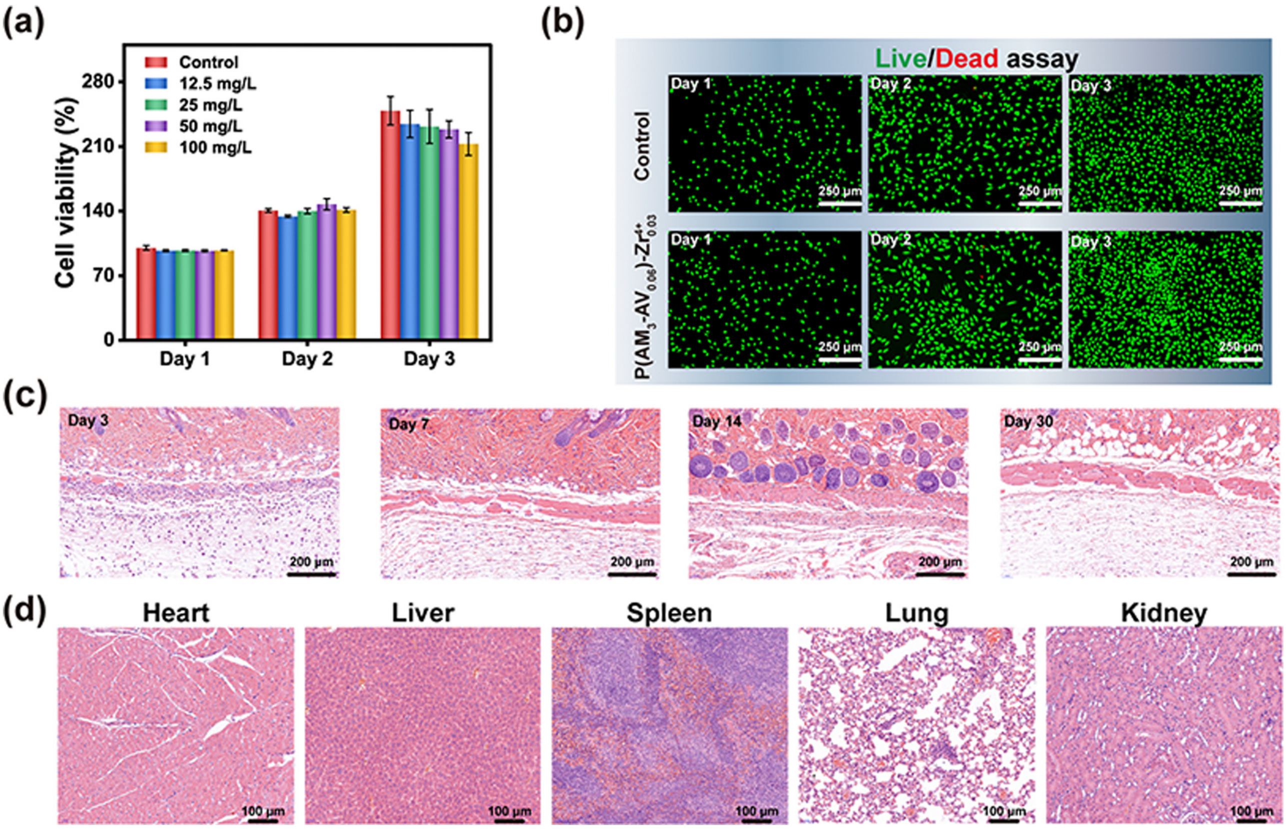

Fig. 6 (a) Relative cell viability of L929 cells cultured with the P($AM_3$–$AV_{0.06}$)–$Zr_{0.03}^{4+}$ hydrogel by MTT assay. (b) Live/dead staining of L929 cells after treatment with 50 mg $mL^{-1}$ P($AM_3$–$AV_{0.06}$)–$Zr_{0.03}^{4+}$ hydrogel extract. The skin tissue (c) and organ (d) biocompatibility of the P($AM_3$–$AV_{0.06}$)–$Zr_{0.03}^{4+}$ hydrogel subcutaneously implanted in the back of mice for 3, 7, 14, and 30 days.

tissue from the implantation site was subjected to H&E staining (Fig. 6c). We found foreign body reaction characterized by neutrophil aggregation and an acute inflammatory response in the initial 7 days, however, the inflammatory reaction subsided, and the tissue gradually returned to be normal 30 days after implantation. Additionally, there was no damage detected on the major organ morphology after 30 days of subcutaneous implantation compared to the normal mice, including the heart, liver, spleen, lung, and kidney, confirming the good biocompatibility of the P($AM_3$–$AV_{0.06}$)–$Zr_{0.03}^{4+}$ hydrogel (Fig. S12, ESI†).

### Sensing performances of P($AM_3$–$AV_{0.06}$)–$Zr_{0.03}^{4+}$ hydrogels

Based on the impressive mechanical and sensing capabilities demonstrated by P($AM_3$–$AV_{0.06}$)–$Zr_{0.03}^{4+}$ hydrogel, it can be effectively utilized as a flexible wearable device for comprehensive human activity monitoring (Fig. 7a).[40] Initially, we employed the P($AM_3$–$AV_{0.06}$)–$Zr_{0.03}^{4+}$ hydrogel to monitor substantial human movements involving the fingers and wrists (Fig. 7b and c). When the hydrogel was affixed to the finger, the $\Delta R/R_0$ progressively increased with the increment of bending angle (from 45° to 135°), and consistent relative resistance changes were recorded for the same bending angles. Similarly, when monitoring elbow bending motions at various degrees of flexion, the hydrogel produced clear and reproducible signals, hunderscoring its reliable sensing capability and potential for accurately detecting a range of rehabilitation exercises (*e.g.*, wrist flexion, elbow flexion, knee flexion, *etc.*).[41] Moreover, the hydrogel-based sensor was capable of capturing subtle movements of the human body. Fig. 7d illustrates the hydrogel's real-time sensing ability in detecting swallowing movements upon attachment to the pharynx, suggesting its potential application in silent human articulation recognition.[42]

Moreover, the P($AM_3$–$AV_{0.06}$)–$Zr_{0.03}^{4+}$ hydrogel showcased remarkable capabilities in monitoring electrophysiological signals, including electrocardiographic signals (ECG) and electromyographic signals (EMG). These signals are vital for monitoring human physiological activities and potentially diagnosing cardiovascular or muscular-related diseases.[43,44] Fig. 7e depicts the high-quality ECG signals recorded when the hydrogel was applied to the subject's left chest, which showed distinct PQRST waveforms. Additionally, the heart rate was determined to be 84 beats per minute indicated by the time interval between adjacent S peaks of the ECG signal (approximately 0.7 seconds), which fell within the normal adult range (60–100 beats per minute). This capability is essential for the prompt and convenient identification of abnormal heart rate signals in humans. Furthermore, clear EMG signals were observed during gripping actions with different weights (1.25, 2.5, and 3.75 kg) (Fig. 7f). The hydrogel-based sensors

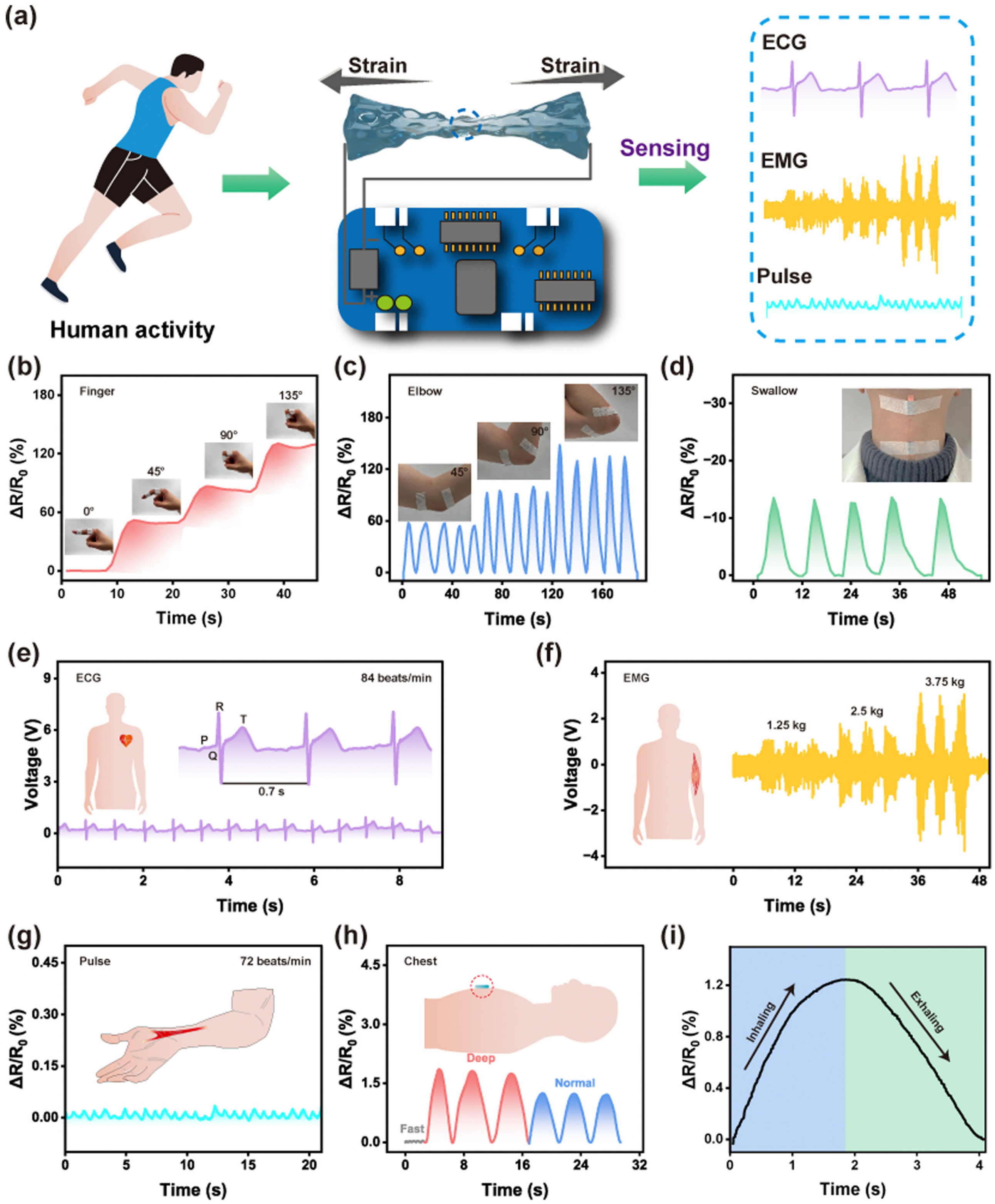

Fig. 7 (a) Schematic diagram of the sensing application of P($AM_3$–$AV_{0.06}$)–$Zr_{0.03}^{4+}$ hydrogel. P($AM_3$–$AV_{0.06}$)–$Zr_{0.03}^{4+}$ hydrogels were used as strain transducers to detect changes in relative resistance when the fingers were bent at different angles (b), the elbow was bent at different angles (c), and swallowing was performed (d). P($AM_3$–$AV_{0.06}$)–$Zr_{0.03}^{4+}$ hydrogel for detection of ECG (e) and EMG (f) signals. (g) P($AM_3$–$AV_{0.06}$)–$Zr_{0.03}^{4+}$ hydrogel for detection of pulse. P($AM_3$–$AV_{0.06}$)–$Zr_{0.03}^{4+}$ hydrogel for detection of chest breathing (h) and (i).

accurately captured different electromechanical signals generated by muscle contractions, exhibiting repetitive and precise measurements. This feature is particularly relevant for monitoring postoperative rehabilitation exercises and treating corresponding damaged muscles.[45] Therefore, $P(AM_3–AV_{0.06})–Zr_{0.03}{}^{4+}$ hydrogels demonstrated immense potential in human health sensing and disease prediction owing to their high electrical conductivity and exceptional sensing capability.

Monitoring the human pulse is essential due to its critical role in providing diagnostic information about heart rate and arterial condition. In Fig. 7g, the application of the $P(AM_3–AV_{0.06})–Zr_{0.03}{}^{4+}$ hydrogel for real-time pulse beat monitoring at the wrist revealed a normal and regular signal waveform with a rate of approximately 72 beats per minute. The frequency and intensity of human respiration are essential features of the body's normal state. Therefore, we positioned the hydrogel-based sensor in the chest area and simulated three distinct respiratory states: fast breathing, deep breathing, and normal breathing, aiming to monitor real-time respiratory changes. As depicted in Fig. 7h and i, monitoring the respiration process in the thoracic region revealed that inhaled gas caused muscle expansion and an increase in thoracic cavity volume, resulting in a stretching state for the hydrogel sensor. This enhanced the electrical signal response, showcasing significant differences in electrical signals across different respiration states.[46] The respiratory rate of normal breathing behaviour, calculated around 20 breaths per minute in the thoracic region, fell within a reasonable range. These findings highlight that the $P(AM_3–AV_{0.06})–Zr_{0.03}{}^{4+}$ hydrogel-based sensor could distinguish respiratory state differences clearly, and may play a pivotal role in monitoring human respiratory states.

## Conclusions

In conclusion, we developed a tough and elastic hydrogel with stable mechanical performances through one-pot radical polymerization of AM, AV and $Zr^{4+}$. Owing to hydrophobicity-assisted metal ion coordination in the network, $P(AM_3–AV_{0.06})–Zr_{0.03}{}^{4+}$ hydrogels with the side group of isopropyl exhibited outstanding mechanical properties compared to $P(AM_3–AG_{0.06})–Zr_{0.03}{}^{4+}$ and $P(AM_3\text{-}AA_{0.06})–Zr_{0.03}{}^{4+}$ hydrogels, including tensile stress of 1.1 MPa, fracture strain of 785% and compression stress of 16 MPa, which also showcased remarkable self-recovery properties and fatigue resistance. Furthermore, the $P(AM_3–AV_{0.06})–Zr_{0.03}{}^{4+}$ hydrogel boasted high electrical conductivity ($1.1\ S\ m^{-1}$), sensitive sensing capabilities (GF = 16.21), and stable electrical signal transmission across multiple stretching and compression processes (500 cycles). These attributes make it highly suitable for comprehensive human activity monitoring, highlighting its immense potential for applications in flexible wearable devices.

## Data availability statement

The data are available from the corresponding author on reasonable request.

## Conflicts of interest

There are no conflicts to declare.

## Acknowledgements

This work was financially supported by the National Natural Science Foundation of China (NSFC 52322309 and 52173139), the ''Young Talent Support Plan'' of Xi'an Jiaotong University, and Fundamental Research Funds for the Central Universities (xzy022023018).

## References

1 J. Y. Yin, S. X. Pan, L. L. Wu, L. Y. N. Tan, D. Chen, S. Huang, Y. H. Zhang and P. X. He, *J. Mater. Chem. C*, 2020, **8**, 17349–17364.

2 S. T. Lin, H. Yuk, T. Zhang, G. A. Parada, H. Koo, C. J. Yu and X. H. Zhao, *Adv. Mater.*, 2016, **28**, 4497–4505.

3 J. Kim, A. S. Campbell, B. E. de Avila and J. Wang, *Nat. Biotechnol.*, 2019, **37**, 389.

4 H. Lee, Y. J. Hong, S. Baik, T. Hyeon and D. H. Kim, *Adv. Healthcare Mater.*, 2018, **7**, e1701150.

5 G. H. Su, J. Cao, X. Q. Zhang, Y. L. Zhang, S. Y. Yin, L. Y. Jia, Q. Q. Guo, X. X. Zhang, J. H. Zhang and T. Zhou, *J. Mater. Chem. A*, 2020, **8**, 2074–2082.

6 Y. Ni, J. Huang, S. Li, X. Wang, L. Liu, M. Wang, Z. Chen, X. Li and Y. Lai, *ACS Appl. Mater. Interfaces*, 2021, **13**, 4740–4749.

7 T. X. Zhu, Y. M. Ni, G. M. Biesold, Y. Cheng, M. Z. Ge, H. Q. Li, J. Y. Huang, Z. Q. Lin and Y. K. Lai, *Chem. Soc. Rev.*, 2023, **52**, 473.

8 Y. S. Zhang and A. Khademhosseini, *Science*, 2017, **356**, eaaf3627.

9 B. Kessel, M. Lee, A. Bonato, Y. Tinguely, E. Tosoratti and M. Zenobi-Wong, *Adv. Sci.*, 2020, **7**, 2001419.

10 T. Zhu, Y. Cheng, C. Cao, J. Mao, L. Li, J. Huang, S. Gao, X. Dong, Z. Chen and Y. Lai, *Chem. Eng. J.*, 2020, **385**, 123912.

11 Q. H. Liu, G. D. Nian, C. H. Yang, S. X. Qu and Z. G. Suo, *Nat. Commun.*, 2018, **9**, 846.

12 G. F. Cai, J. X. Wang, K. Qian, J. W. Chen, S. H. Li and P. S. Lee, *Adv. Sci.*, 2017, **4**, 1600190.

13 H. Kamata, K. Kushiro, M. Takai, U. Chung and T. Sakai, *Angew. Chem., Int. Ed.*, 2016, **55**, 9282–9286.

14 K. Xu, K. X. Shen, J. Yu, Y. X. Yang, Y. T. Wei, P. L. Lin, Q. Zhang, C. H. Xiao, Y. F. Zhang and Y. L. Cheng, *Chem. Mater.*, 2022, **34**, 3311–3322.

15 J. Yu, K. Xu, X. J. Chen, X. D. Zhao, Y. X. Yang, D. K. Chu, Y. L. Xu, Q. Zhang, Y. F. Zhang and Y. L. Cheng, *Biomacromolecules*, 2021, **22**, 1297–1304.

16 X. H. Meng, Y. Qiao, C. W. Do, W. Bras, C. Y. He, Y. B. Ke, T. P. Russell and D. Qiu, *Adv. Mater.*, 2022, **34**, 2108243.

17 C. Liu, N. Y. Morimoto, L. Jiang, S. Kawahara, T. Noritomi, H. Yokoyama, K. Mayumi and K. Ito, *Science*, 2021, **372**, 1078–1081.

18 M. Y. Zhang, Y. X. Yang, M. Li, Q. H. Shang, R. L. Xie, J. Yu, K. X. Shen, Y. F. Zhang and Y. L. Cheng, *Adv. Mater.*, 2023, **35**, 2301551.

19 G. Janarthanan and I. Noh, *J. Mater. Sci. Technol.*, 2021, **63**, 35–53.

20 F. Gao, Y. Y. Zhang, Y. M. Li, B. Xu, Z. Q. Cao and W. G. Liu, *ACS Appl. Mater. Interfaces*, 2016, **8**, 8956–8966.

21 K. X. Shen, K. Xu, M. Y. Zhang, J. Yu, Y. X. Yang, X. D. Zhao, Q. Zhang, Y. S. Wu, Y. F. Zhang and Y. L. Cheng, *Chem. Eng. J.*, 2023, **451**, 138525.

22 H. C. Yu, S. Y. Zheng, L. T. Fang, Z. M. Ying, M. Du, J. Wang, K. F. Ren, Z. L. Wu and Q. Zheng, *Adv. Mater.*, 2020, **32**, 2005171.

23 L. Y. Shi, P. H. Ding, Y. Z. Wang, Y. Zhang, D. Ossipov and J. Hilborn, *Macromol. Rapid Commun.*, 2019, **40**, 1800837.

24 L. Hu, Y. X. Wang, Q. Liu, M. Liu, F. M. Yang, C. X. Wang, P. P. Pan, L. Wang, L. Chen and J. D. Chen, *Chin. Chem. Lett.*, 2023, **32**, 108262.

25 Y. Hu, Z. S. Du, X. L. Deng, T. Wang, Z. H. Yang, W. Y. Zhou and C. Y. Wang, *Macromolecules*, 2016, **49**, 5660–5668.

26 Y. Wang, Y. J. Xie, X. Y. Xie, D. Wu, H. T. Wu, X. Q. Luo, Q. Wu, L. J. Zhao and J. R. Wu, *Adv. Funct. Mater.*, 2023, **33**, 2210224.

27 Y. Ma, M. Hua, S. Wu, Y. Du, X. Pei, X. Zhu, F. Zhou and X. He, *Sci. Adv.*, 2020, **6**, eabd2520.

28 Y. Gao, K. Wu and Z. Suo, *Adv. Mater.*, 2019, **31**, 1806948.

29 H. C. Yu, X. P. Hao, C. W. Zhang, S. Y. Zheng, M. Du, S. M. Liang, Z. L. Wu and Q. Zheng, *Small*, 2021, **17**, 2103836.

30 J. J. Max and C. Chapados, *J. Phys. Chem. A*, 2004, **108**, 3324.

31 V. Nigro, F. Ripanti, R. Angelini, A. Sarra, M. Bertoldo, E. Buratti, P. Postorino and B. Ruzicka, *J. Mol. Liq.*, 2019, **284**, 718.

32 W. X. Sun, B. Xue, Q. Y. Fan, R. H. Tao, C. X. Wang, X. Wang, Y. R. Li, M. Qin, W. Wang, B. Chen and Y. Cao, *Sci. Adv.*, 2020, **6**, eaaz9531.

33 T. L. Sun, T. Kurokawa, S. Kuroda, A. B. Ihsan, T. Akasaki, K. Sato, M. A. Haque, T. Nakajima and J. P. Gong, *Nat. Mater.*, 2013, **12**, 932.

34 C. Du, X. N. Zhang, T. L. Sun, M. Du, Q. Zheng and Z. L. Wu, *Macromolecules*, 2021, **54**, 4313.

35 S. Y. Zheng, H. Ding, J. Qian, J. Yin, Z. L. Wu, Y. Song and Q. Zheng, *Macromolecules*, 2016, **49**, 9637.

36 H. Y. Liu, X. Wang, Y. X. Cao, Y. Y. Yang, Y. T. Yang, Y. F. Gao, Z. S. Ma, J. F. Wang, W. J. Wang and D. C. Wu, *ACS Appl. Mater. Interfaces*, 2020, **12**, 25334–25344.

37 G. H. Su, Y. L. Zhang, X. Q. Zhang, J. Feng, J. Cao, X. X. Zhang and T. Zhou, *Chem. Mater.*, 2022, **34**, 1392–1402.

38 J. J. Wei, Y. F. Zheng and T. Chen, *Mater. Horiz.*, 2021, **8**, 2761–2770.

39 K. X. Shen, Z. Liu, R. L. Xie, Y. C. Zhang, Y. X. Yang, X. D. Zhao, Y. F. Zhang, A. M. Yang and Y. L. Cheng, *Mater. Horiz.*, 2023, **10**, 2096–2108.

40 S. Bao, J. Gao, T. Xu, N. Li, W. Chen and W. Lu, *Chem. Eng. J.*, 2021, **411**, 128470.

41 A. Schaefer, H. Horn and R. Ahlrichs, *J. Chem. Phys.*, 1992, **97**, 2571.

42 M. K. Li, Y. F. Zhang, L. S. Y. Lian, K. Liu, M. Lu, Y. B. Chen, L. Q. Zhang, X. C. Zhang and P. B. Wan, *Adv. Funct. Mater.*, 2022, **32**, 2208141.

43 Z. Lei, W. Zhu, X. Zhang, X. Wang and P. Wu, *Adv. Funct. Mater.*, 2021, **31**, 2008020.

44 H. Xia, H. Tang, B. Zhou, Y. Li, X. Zhang, Z. Shi, L. Deng, R. Song, L. Li, Z. Zhang and J. Zhou, *Sens. Actuators*, 2020, **312**, 127962.

45 L. Zhang, K. S. Kumar, H. He, C. J. Cai, X. He, H. Gao, S. Yue, C. Li, R. C. Seet, H. Ren and J. Ouyang, *Nat. Commun.*, 2020, **11**, 4683.

46 J. Liu, H. Y. Wang, T. Liu, Q. A. Wu, Y. H. Ding, R. X. Ou, C. G. Guo, Z. Z. Liu and Q. W. Wang, *Adv. Funct. Mater.*, 2022, **32**, 2204686.